Monthly Notices
of the
ROYAL ASTRONOMICAL SOCIETY

MNRAS **433,** 1287–1299 (2013) doi:10.1093/mnras/stt811
Advance Access publication 2013 June 3

Dust-obscured star formation in the outskirts of XMMU J2235.3−2557, a massive galaxy cluster at $z = 1.4$*

J. S. Santos,[1]† B. Altieri,[1] P. Popesso,[2] V. Strazzullo,[3] I. Valtchanov,[1] S. Berta,[2] H. Böhringer,[2] L. Conversi,[1] R. Demarco,[4] A. C. Edge,[5] C. Lidman,[6] D. Lutz,[2] L. Metcalfe,[1] C.R. Mullis,[7] I. Pintos-Castro,[8,9,10] M. Sánchez-Portal,[1] T. D. Rawle,[1] P. Rosati,[11] A. M. Swinbank[5] and M. Tanaka[12]

[1]*European Space Astronomy Centre (ESAC)/ESA, Villanueva de la Cañada, E-28691 Madrid, Spain*
[2]*Max-Planck-Institut für extraterrestrische Physik, Giessenbachstraße, D-85748 Garching, Germany*
[3]*CEA Saclay, Service d'Astrophysique, L'Orme des Merisiers, Bât. 709, F-91191 Gif-sur-Yvette Cedex, France*
[4]*Department of Astronomy, Universidad de Concepcion, Casila 160-C, Concepcin, Chile*
[5]*Department of Physics, Durham University, Durham DH1 3LE, UK*
[6]*Australian Astronomical Observatory, PO Box 915, North Ryde, NSW 1670, Australia*
[7]*Wachovia Corporation, NC6740, 100 N. Main Street, Winston-Salem, NC 27101, USA*
[8]*Instituto de Astrofísica de Canarias, La Laguna, Tenerife, Spain*
[9]*Departamento de Astrofísica, Facultad de Física, Universidad de La Laguna, La Laguna, Tenerife, Spain*
[10]*Centro de Astrobiología, INTA-CSIC, Villanueva de la Cañada, Madrid, Spain*
[11]*European Southern Observatory (ESO), Garching, Germany*
[12]*Institute for the Physics and Mathematics of the Universe, The University of Tokyo, 5-1-5 Kashiwanoha, Kashiwa-shi, Chiba 277-8583, Japan*

Accepted 2013 May 7. Received 2013 April 19; in original form 2013 March 8

ABSTRACT

Star formation (SF) in the galaxy populations of local massive clusters is reduced with respect to field galaxies, and tends to be suppressed in the core region. Indications of a reversal of the SF–density relation have been observed in a few $z > 1.4$ clusters. Using deep imaging from 100–500 μm from Photodetector Array Camera and Spectrometer (PACS) and Spectral and Photometric Imaging REceiver (SPIRE) onboard *Herschel*, we investigate infrared properties of spectroscopic and photo-z cluster members, and of Hα emitters in XMMU J2235.3−2557, one of the most massive, distant, X-ray selected clusters known. Our analysis is based mostly on fitting of the galaxies spectral energy distribution (SED) in the rest-frame 8–1000 μm. We measure total IR luminosity, deriving star formation rates (SFRs) ranging from 89 to 463 $\mathrm{M}_\odot\,\mathrm{yr}^{-1}$ for 13 galaxies individually detected by *Herschel*, all located beyond the core region ($r > 250$ kpc). We perform a stacking analysis of nine star-forming members not detected by PACS, yielding a detection with SFR $= 48 \pm 16\,\mathrm{M}_\odot\,\mathrm{yr}^{-1}$. Using a colour criterion based on a star-forming galaxy SED at the cluster redshift, we select 41 PACS sources as candidate star-forming cluster members. We characterize a population of highly obscured SF galaxies in the outskirts of XMMU J2235.3−2557. We do not find evidence for a reversal of the SF–density relation in this massive, distant cluster.

Key words: galaxies: clusters: individual: XMMU J2235.3-2557 – galaxies: high-redshift – galaxies: star formation – infrared: galaxies.

1 INTRODUCTION

The high-density environments of galaxy clusters are ideal laboratories to study the formation and evolution of galaxies. A wide range of physical mechanisms takes place in these nodes of the cosmic web, namely galaxy harassment, tidal and ram pressure stripping and mergers, that result in a population of galaxies with a diverse range of properties. However, two distinct families stand out, the early-types or passive galaxies, and the late-types or star-forming galaxies. While the cores of nearby massive galaxy clusters are typically dominated by red, passive galaxies with old stellar populations, star-forming galaxies are usually located at the cluster outskirts, where the quenching mechanisms are no longer dominant (e.g. Treu et al. 2003; Haines et al. 2007).

---

* Based on observations with *Herschel*, an ESA space observatory with science instruments provided by European-led Principal Investigator consortia and with important participation from NASA.

† E-mail: jsantos@sciops.esa.int

Published by Oxford University Press on behalf of the Royal Astronomical Society

The high-mass end of the galaxy populations in clusters appears to be dominated by quiescent, early-type galaxies, even up to $z = 1.4$ (e.g. Lidman et al. 2008). However, as we approach the global cosmic star formation density peak ($1 < z < 2$), we expect an enhancement of star formation (SF) to take place in the biased environments of clusters, the so-called reversal of the SF–density relation (Dressler 1980). The identification of the epoch when these massive galaxies showed the first signs of SF as a function of galaxy mass, environmental density and cluster halo mass can set tight constraints on structure formation models (Hopkins et al. 2008; De Lucia et al. 2010). Still, the details (i.e. fraction and location of star-forming galaxies and amount of SF) of this increase remain unclear.

Most of the energy from SF and active galactic nuclei (AGN) activity is absorbed by dust and re-radiated in the infrared. Prior to the advent of orbital infrared observatories such as *Infrared Space Observatory* (*ISO*), *Akari* and *Spitzer*, one of the most widely used methods for determining SFRs in galaxies had been through measurements of the Hα 6563 Å luminosity (Kennicutt 1998; Kewley et al. 2002). However, extending this method to high redshifts is challenging due to the difficulties of obtaining ground-based near-infrared (NIR) spectroscopy of faint galaxies. In the absence of Hα, SF is usually quantified via the [O II] λ 3727 emission line (Heckman et al. 1989; Hayashi et al. 2010), although a degree of uncertainty exists about the reliability of [O II] as a SF tracer (Coia et al. 2005; Lemaux et al. 2010), as it is sensitive to dust extinction and metallicity, as well as being enhanced in low-ionization nuclear emission-line regions (LINERs).

Observations with *ISO* (Coia et al. 2005; Metcalfe, Fadda & Biviano 2005) and later on with MIPS onboard *Spitzer* provided a significant development in understanding SF in galaxies at intermediate redshift. Saintonge, Tran & Holden (2008) observed a significant increase in the fraction of dusty star-forming cluster galaxies up to $z = 0.83$ (now dubbed the MIR Butcher–Oemler effect). Mid-infrared observations of galaxy clusters at the highest known redshifts ($z \sim 1.5$) have begun to reveal a population of IR luminous, actively star-forming galaxies deep within the cluster cores (Hilton et al. 2010; Tran et al. 2010). In particular, *Spitzer*/MIPS 24 µm observations of the moderately massive cluster XCS J2215−1738 at $z = 1.46$, show that this cluster hosts a significant population of galaxies with very high SFRs, even in core region (Hilton et al. 2010).

The *Herschel* observatory (Pilbratt et al. 2010) is the largest space telescope to date and provides unrivalled sensitivity in the wavelength window ranging from 55 to 672 µm. *Herschel* brackets the critical peak of far-infrared (FIR) emission of $z \sim 1$–2 galaxies, providing a direct, unbiased measurement of SF. Several *Herschel* Key Projects were designed to measure the SF activity at high redshift and to investigate the role of environment in regulating the SF activity. In particular, results from the Photodetector Array Camera and Spectrometer (PACS) Evolutionary Probe Key Project (PEP; Lutz et al. 2011) indicate that for massive galaxies ($M/M_{\odot} > 10^{11}$) at $z \sim 1$ the mean specific star formation rate (SFR) tends to be higher at higher density (Popesso et al. 2011).

Using recently acquired *Herschel* imaging data, we present in this paper a detailed account of the dust-obscured SF properties in the galaxy population of the X-ray selected cluster XMMU J2235.3−2557 (hereafter XMM2235) at $z = 1.393$ (Mullis et al. 2005). This massive, distant cluster was discovered by the *XMM–Newton* Distant Cluster Project (see Fassbender et al. 2011 for a recent review of the survey results). Given its remarkable position in redshift and its high mass (Jee et al. 2009), XMM2235 has been the subject of deep, multiwavelength follow-up observations using the major astronomical observatories. NIR $J/K_{\rm s}$ data obtained with HAWK-I revealed a tight red sequence with a low scatter in the $J - K_{\rm s}$ colour–magnitude relation (Lidman et al. 2008) and a clear segregation between the core, red galaxies and the outer, bluish galaxies. Using *Hubble Space Telescope* (*HST*)/ACS and NICMOS optical/NIR data, the properties of the passive cluster galaxies have been accurately studied (Strazzullo et al. 2010), indicating that SF appears to be effectively suppressed in the cluster centre ($r < 250$ kpc). Furthermore, the spectral energy distribution (SED)-derived SF ages confirmed an old population of galaxies with $z_{\rm form} > 3$ in the inner core and a significant younger population in the outskirts (Rosati et al. 2009). These studies show that despite the lookback time of 9 Gyr, XMM2235 has an evolved galaxy population, with a massive brightest cluster galaxy (BCG). More recently, a narrow-band imaging survey searching for Hα emitters (Bauer et al. 2011; Grützbauch et al. 2012) added further investigation on the SF properties of the cluster galaxy population.

The paper is organized as follows: in Section 2 we describe the PACS and Spectral and Photometric Imaging REceiver (SPIRE) observations and reduction procedures. In Section 3 we describe the extensive multi-wavelength ancillary data used in this study. We perform the SED fitting of individual detections in Section 4 to derive the FIR properties of the cluster galaxies, namely, the total FIR luminosity, L_{IR}, SFR and specific star formation rate (sSFR). In Section 5, we perform a stacking analysis of the non-detections and in Section 6, we present the sSFR–stellar mass relation. The presence of X-ray AGNs in our sample and their luminosity is quantified in Section 7. Using the high-resolution *HST*/ACS data, we determine the morphologies of the cluster members with *Herschel* detection in Section 8. Based on the FIR SED shape of the sources, we define a sample of PACS cluster candidates in Section 9. In Section 10, we present the analysis of the integral field unit (IFU) SINFONI spectroscopy data of the BCG. Our conclusions are summarized in Section 11.

The cosmological parameters used throughout the paper are: $H_0 = 70$ km s^{-1} Mpc^{-1}, $\Omega_{\Lambda} = 0.7$ and $\Omega_{\rm m} = 0.3$. Magnitudes are reported in the AB system and we will use the Salpeter initial mass function (IMF) unless otherwise stated.

2 *HERSCHEL* OBSERVATIONS AND DATA REDUCTION

The *Herschel* observations of XMM2235 were carried out as part of two programmes, one in guaranteed time (GT1, PI Altieri) and one in open time 1 (OT1, PI Popesso).

The PACS 100/160 µm imaging data were taken within the scope of the 100 h OT1 programme designed to study the FIR SF history of a sample of eight X-ray selected galaxy clusters at $1.4 < z < 1.8$, and investigate the relation between SF activity and environment at the epoch when clusters are assembling galaxies at a faster rate than today and galaxies are still undergoing their own formation process. The results obtained for the complete cluster sample observed in this programme will be presented in forthcoming papers.

The SPIRE 250/350/500 µm imaging data were taken in the context of the smaller and shallower GT1 programme, aimed at studying the evolution of SF in eight high-redshift clusters within the range $0.8 < z < 2.4$, including two well-known proto-clusters (see Seymour et al. 2012, Sanchez-Portal et al., in preparation). This programme complements the one observed in OT1, by increasing sample statistics and extending it to higher redshift.

2.1 PACS observations and catalogue

The PACS (Poglitsch et al. 2011) observations were acquired in December 2011 (ObsId = 1342234105, 1342234106, 1342234430, 1342234431), amounting to a total of ∼24 h. The full data reduction of the data considered here in addition to the full data set of the original PACS Program are described in Popesso et al. (in preparation). Here we summarize the main steps. Data are processed through the standard PACS data reduction pipeline in the Hipe environment (Ott et al. 2006), with the addition of some custom procedures, aimed at removal of instrument artefacts. These procedures comprise: iterative masking of the sources for avoiding residuals due to the high-pass filtering implemented in the PACS pipeline. Visual inspection of scan legs to flag and discard scan legs affected by interferences in the blue channel. Offsets and errors in the pointing of the *Herschel* satellite are corrected by re-centring the data on a grid of known bright priors. The map coaddition and error estimation is performed through a weighted mean of several maps with the same WCS. The PACS catalogues at 100 and 160 μm are created via a blind extraction using the STARFINDER PSF-fitting code (Diolaiti et al. 2000). Flux reliability, incompleteness and spurious source fraction are estimated and tested via Monte Carlo simulations. Dedicated IDL procedures, described in Popesso et al. (2012) are used to check the effect of the high-pass filtering task on the source flux in different flux bins by adding fake sources on the PACS pixel timeline. See also Berta et al. (2011), Lutz et al. (2011) for further details about source extraction and data reduction. The images have a pixel scale of 1.2 arscec pix^{-1} and 2.4 arscec pix^{-1} in the 100 μm and 160 μm bands, respectively. The PACS point spread function (PSF) at the nominal scan speed (20 arscec s^{-1}) is 6.7 arscec at 100 μm and 11.3 arscec at 160 μm.

The PACS 3σ blind detection catalogues have 344 in the 100 μm band and 298 sources in the 160 μm band, with corresponding 3σ sensitivity limits of 2.25 and 4.5 mJy, respectively. We cross-matched the two blind catalogues using a nearest neighbour algorithm with a cross-match distance of 5 arcsec to obtain a catalogue with 158 sources that are present in both PACS bands. We use this catalogue as prior for extracting sources in the SPIRE images.

2.2 SPIRE observations and catalogue

The SPIRE (Griffin et al. 2010) observations (ObsID: 1342210530, 34 min exposure) were performed using a cross-scan Large Map mode over a 10 × 10 arcmin region with four repetitions, achieving 1σ instrumental noise (3.5, 4.8, 5.4) mJy at (250, 350, 500) μm – slightly below the SPIRE extragalactic confusion noise, (5.8, 6.3, 6.8) mJy at (250, 350, 500) μm (Nguyen et al. 2010) in the three SPIRE bands. The standard SPIRE map making was used to generate the maps from the SPIRE bolometers timelines. To get SPIRE photometry for sources in XMM2235, we used SUSSEXTRACTOR 10.0.836, a source detection method developed for SPIRE maps (Smith et al. 2012) to produce a catalogue based on priors from PACS. For non-detections, we consider 3σ upper limits of 17.4 mJy, 18.9 mJy and 20.4 mJy at 250, 350 and 500 μm, respectively, including confusion noise and the flux calibration uncertainties. The beam full width at half-maximum (FWHM) on our standard maps are (18, 25, 36) arcsec at (250, 350, 500) μm.

Using the 3σ flux limits in all five *Herschel* bands, we obtain an estimate of the lower limit on the SFR for these observations at $z = 1.4$. We thus obtain a 3σ SFR equal to 105 $\mathrm{M}_{\odot}\,\mathrm{yr}^{-1}$, based on the *Herschel* observations for this cluster.

3 ANCILLARY MULTIWAVELENGTH DATA

The galaxy cluster XMM2235 benefits from an extensive multi-wavelength coverage, including deep, high-resolution X-ray data from *Chandra*, optical imaging with the *HST*, NIR imaging with VLT/HAWK-I and spectroscopic data with VLT/FORS2 taken over a large field of view (FOV). Details on the optical and NIR data used here can be found in Strazzullo et al. (2010) and Lidman et al. (2008), respectively. The high-quality, high-resolution K_s-band data obtained over a large FOV (13.5 arcmin × 13.5 arcmin) nearly matches the area covered with PACS. This broad data set is fundamental to the analysis of the *Herschel* data which suffer from blending, and confusion only in the longest wavelengths.

For our analysis, we use an extensive spectroscopic campaign based on four VLT/FORS2 masks using both the MOS and MXU modes, described in Rosati et al. (2009). The catalogue with 209 spectroscopic redshifts will be published in Strazzullo et al. (in preparation). The targets were initially selected using colours and magnitudes aiming at the detection of red members (Mullis et al. 2005). Fainter objects with colours consistent with late- and early-type galaxies at the cluster redshift were targeted in subsequent masks (Rosati et al. 2009). To date, a total of 35 cluster members have been confirmed within a redshift range $1.374 < z < 1.406$, and about a third of these (11) have a clear detection of the [O II] λ 3727 emission line.

In addition to the spectroscopic catalogue, we also use photometric redshifts computed with the *U, R, i, z, J, H, K* bands, to overcome any bias or incompleteness of the spectroscopic sample and thus consider all galaxies which might be cluster members. The photo-z catalogue encompasses the central ∼5 arcmin × 3 arcmin, where we have optimal optical/NIR photometric coverage. The scatter of these photometric redshifts is $\delta z/(1 + z) < 6$ per cent, with an estimated contamination by interlopers of 50 per cent (obtained by comparison with the spectroscopic catalogue). The photometric redshift range used for selecting cluster members is $1.1 \le z \le 1.7$. All the details concerning this catalogue are found in Strazzullo et al. (2010).

We also use here the recently published catalogue of 163 narrow-band emitters detected in two narrow-band imaging pointings with NIRI on *GEMINI*/North, covering mostly the central part (3.5 arcmin × 5 arcmin) of the cluster (Grützbauch et al. 2012). The *H* narrow-band filter centred at a wavelength of 1.57 μm and with a width of 232 Å allows for the detection of the Hα λ6563 line in the redshift range [1.372–1.408]. To ensure a robust analysis of these sources we opted to use only those which have an Hα-derived SFR ≥ 5.5 M⊙ yr^{-1}, the 5σ upper limit quoted by the authors computed with an Hα extinction of 1 mag. A total of 59 Hα sources fulfil this criterion (see footprint of the narrow-band sources in Fig. 1) and will be used in our analysis. Using our extensive spectroscopic and photo-z catalogues, we find that 25 narrow-band emitters are cluster members (of which 10 have spectroscopic redshift), and 14 are interlopers (of which 7 have spectroscopic redshift). For the remaining 20 narrow-band emitters, we do not have redshift information. We would expect a higher correspondence between the Hα galaxy candidates and our FIR data, relative to the spectroscopically confirmed members, since the former are mostly star forming by definition. There is, nonetheless, the possibility that extinction plays a prominent role, preventing highly star-forming galaxies to be seen in the narrow-band observations.

We use the *Spitzer*/IRAC data taken in 2005 (PI C.R. Mullis, prog ID 20760), which is important to ensure a proper identification of the sources seen in *Herschel* and link them to the optical/NIR. The four-channel data were retrieved from the archive and reduced

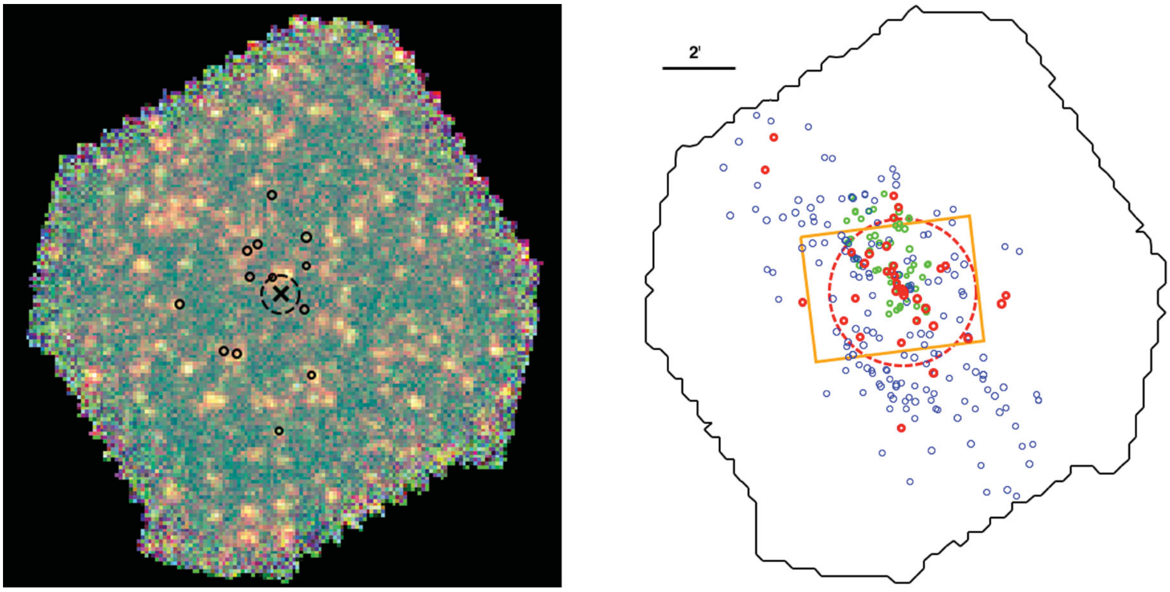

Figure 1. Left: PACS+SPIRE RGB (250/160/100 μm) image of XMM2235 centred on the cluster X-ray centre (black cross). The black circle indicates a radius of 250 kpc centred on the BCG. The 13 cluster members with FIR emission (see Table 2) are shown with small circles. Right: PACS 100 μm footprint (black contour) displaying the complete spectroscopic catalogue (blue), the 35 confirmed cluster members (red) and the 59 Hα emitters (green). The area with photometric redshifts in enclosed by the orange rectangle and the red dashed circle indicates a radius of 1 Mpc centred on the BCG. The images have a size of $15.5' \times 15.5'$. North is up and East is to the left.

with standard procedures. Source extraction was performed in point response function (PRF) multiframe mode within APEX. The PRFs used in the process were the default ones provided by the *Spitzer* Science Centre. The data processing was performed with the tool `mopex` 18.5 using the standard parameters included in the `mopex` pipeline provided by the *Spitzer* helpdesk. We perform blind source extraction for each band and PSF-fitting photometry using `mopex`. Sources below the 5σ detection thresholds ([0.0044, 0.0045, 0.0060, 0.0062] mJy at [3.6, 4.5, 5.8, 8] μm, respectively) were discarded.

XMM2235 was observed with the *Chandra* ACIS–S detector in VFAINT mode with a total effective exposure time of 196 ks (PI Mullis). The full data analysis and reduction were published in Rosati et al. (2009). The sub-arcsecond resolution of *Chandra* allows for a robust detection of point sources, and therefore it is important for our work in identifying AGN contamination in members with FIR emission (see Section 7).

Lastly, we describe and analyse in Section 8 the deep IFU spectroscopy data of the BCG obtained with SINFONI at the VLT, aimed at detecting SF in the BCG through the detection of the Hα emission line. In Table 1, we summarize the data used in this paper.

Table 1. Summary of the data sets used in our analysis. The ‘Type’ column refers to spectroscopy (S) or imaging (I).

Instrument	Type	Observed Band	Field of view
FORS2	S	R, z (MOS/MXU)	6.5 arcmin × 13 arcmin
ACS	I	F850LP	3.5 arcmin × 3.5 arcmin
NIRI	I	H narrow	3 arcmin × 4 arcmin
HAWK-I	I	J, K_s	13.5 arcmin × 13.5 arcmin
SINFONI	S	H	8 arcmin × 8 arcmin
IRAC	I	3.6/4.5/5.8/8.0 μm	14.5 arcmin × 8 arcmin
PACS	I	100/160 μm	11 arcmin × 11 arcmin
SPIRE	I	250/350/500 μm	16 arcmin × 16 arcmin
ACIS-S	I	0.5–10 keV	8.5 arcmin × 9 arcmin

4 FIR SED FITTING OF INDIVIDUAL DETECTIONS

In this section, we perform a standard SED-fitting of the infrared range with the widely used SED fitting code LEPHARE (Arnouts et al. 1999; Ilbert et al. 2006) that is based on a χ^2 minimization. We use the suite of infrared galaxy templates published by Chary & Elbaz (2001) (CE01) for the rest-frame 8–1000 μm range, and Bruzual & Charlot (2003) templates (BC03) for the NIR part of the spectra.

To ensure a proper identification of the cluster members in the *Herschel* maps, we first performed a visual identification of all member galaxies in the K_s, IRAC and PACS images (see Figs 2 and 3). We then matched the PACS catalogue with the spectrophotometric catalogues using a nearest match algorithm with a search radius of 5 arcsec. Blending affects some of the detections making a precise decontamination too difficult. In such cases, we take the following considerations to evaluate whether the FIR emission originates from the cluster member: (i) check whether the cluster member has [O II] or Hα emission as an indication of SF, (ii) investigate the properties of the contaminants using our spectrophotometric catalogues, (iii) evaluate the spatial separation between the target galaxy and contaminant and how the relative emission of the galaxies evolves from the K band, 8 μm, 100 μm to the 160 μm images (see Figs 2 and 3). Based on these considerations, we rejected three of nine spectroscopic members detected either in the matched 100–160 μm catalogue or in the single band detections for which we performed manual photometry. In addition to the spectroscopic members, we also investigate the FIR properties of the galaxies with photometric redshift consistent with the cluster redshift, i.e. within 2σ of the cluster redshift ($1.1 \le z \le 1.7$). Following the same procedure, we find a total of eight photo-z members in the 3σ PACS catalogue (see Tables 2 and 3). The galaxy ID 5 is common to both the spectroscopic and photometric redshift catalogue. With the exception of this cluster member, all sources lie at a distance greater than 250 kpc (equal to a third of R_{500}) from the cluster X-ray centre. Half of the

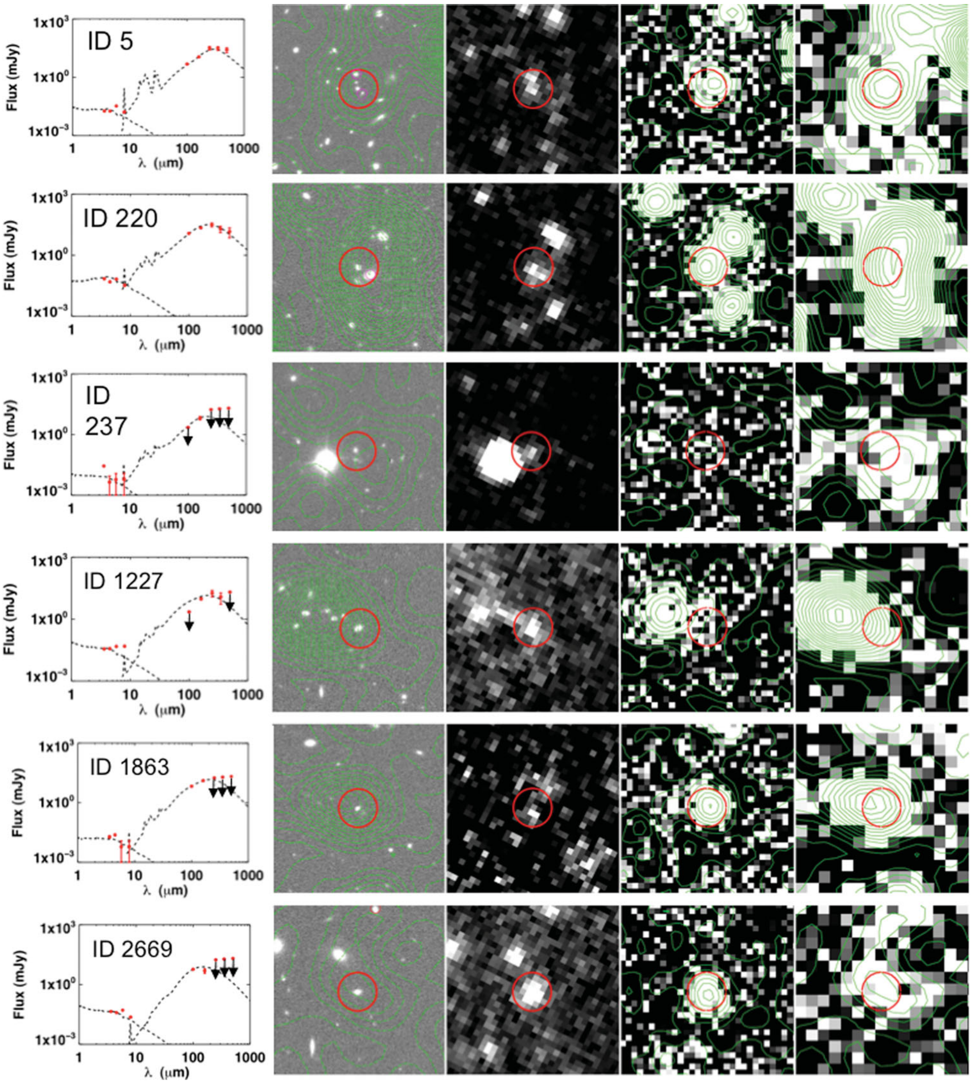

Figure 2. Gallery of the six spectroscopically confirmed cluster members with *Herschel* detection. For each galaxy, we show the FIR SED best fit in the observed frame, and stamps with 35 arcsec × 35 arcsec of the *K*-band with 160 μm contours overlaid in green, 8 μm, 100 μm and 160 μm band (ordered left to right). The red circles have a radius of 4 arcsec. The exact positions of the PACS blind detection catalogue used in the flux measurements are not shown to avoid crowding, as they mostly overlap with the red circles.

spectroscopic members show the [O II] signature in their spectra and the four cluster members detected by PACS with ID 5, 237, 1227 and 2669 have X-ray emission indicating AGN activity (see Section 7). As indicated in Table 2, the FIR emission assigned to some cluster galaxies may be contaminated by background or foreground galaxies. In such cases, the measured SFR should be interpreted as an upper limit, since only dedicated NIR spectroscopy will allow us to properly identify the star-forming galaxies.

The total IR luminosities, $L(8\text{–}1000\,\mu\mathrm{m})$ of the 13 individual galaxy members are computed with LEPHARE by integrating the best-fitting SED models. Using Kennicutt (1998) that assumes a Salpeter IMF, we obtain the SFR with the following conversion:

$$\mathrm{SFR}\,(\mathrm{M}_\odot\,\mathrm{yr}^{-1}) = 4.5 \times 10^{-44} L_{\mathrm{IR}}\,(\mathrm{erg\,s}^{-1}). \quad (1)$$

Luminous infrared galaxies (LIRGs) are defined as having $10^{11} < L_{\mathrm{IR}}/\mathrm{L}_\odot < 10^{12}$ and Ultra luminous infrared galaxies (ULIRGs) have a luminosity greater than 10^{12} $\mathrm{L}_\odot$. The cluster galaxies cover the range of infrared luminosities $0.5 \times 10^{12} < L_{\mathrm{IR}}/\mathrm{L}_\odot < 2.7 \times 10^{12}$, with about one third of the galaxies in the LIRG range and the remaining 2/3 are ULIRGS. In comparison with earlier work on five nearby, massive clusters with *ISO* data (Metcalfe et al. 2005) in which no ULIRG was found among 35 cluster member detections, and more recent work (Haines et al., submitted) using *Herschel* observations of a larger sample of 30 clusters with only one to two detected ULIRGs, the fraction of ULIRGs in this distant cluster suggests a significant increase in the number of ULIRGs with redshift.

We measure SFRs in the range $89 \pm 35 < \mathrm{SFR}\,(\mathrm{M}_\odot\,\mathrm{yr}^{-1}) < 463 \pm 44$ for our 13 spectroscopic and photometric redshift cluster members. To investigate the spatial distribution of the SF members, we sum the galaxies SFRs binned in three radial annuli: $250 < r_1 < 500$ kpc, $500 < r_2 < 1$ Mpc, $r_3 > 1$ Mpc. As shown in Fig. 4, most of the cluster FIR SF occurs at a cluster centric radius larger than 1 Mpc, indicating that the cluster galaxy infalling regions are the most active locations in this cluster.

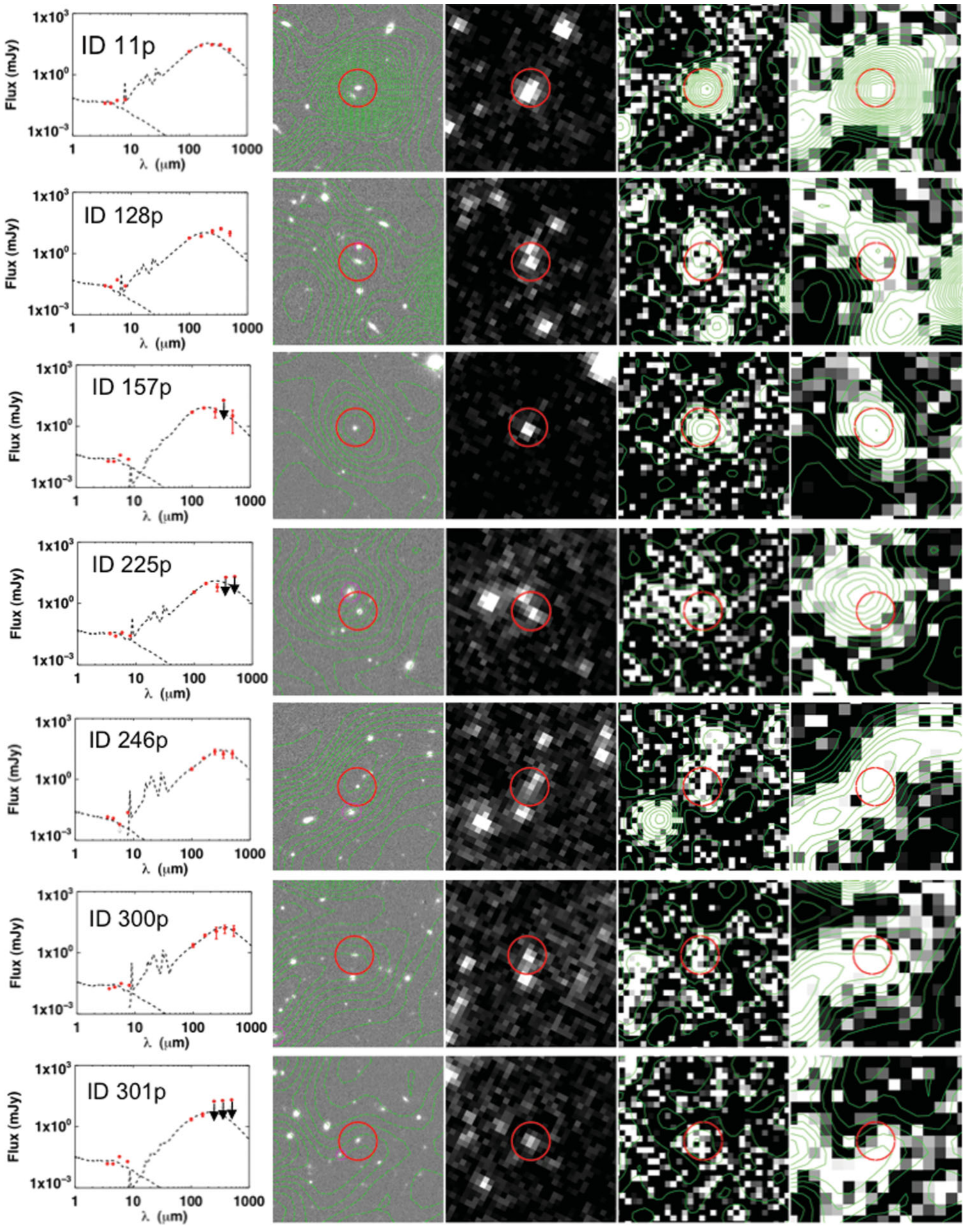

Figure 3. Gallery of the seven photometric redshift cluster members with *Herschel* detection. For each galaxy we show the FIR SED best fit in the observed frame, and stamps with 35 arcsec × 35 arcsec of the *K*-band with 160 μm contours overlaid in green, 8 μm, 100 μm and 160 μm band (ordered left to right). The red circles have a radius of 4 arcsec.

5 STACKING ANALYSIS

In addition to the study of the cluster galaxies individually detected by PACS, we also constrained the SF of the cluster members that are potentially star forming but do not have a detection in the FIR, as has been done in e.g., Dole et al. (2006). We performed a mean stacking analysis using the IDL stacking software of Bethermin et al. (2010) and Bavouzet (2008) on the residual maps at 100 μm and 160 μm of two samples without PACS detection: (1) the spectroscopically confirmed members with indications of on-going SF, and (2) the narrow-band emitters with a spectroscopic or photometric redshift within 2σ from the cluster redshift. We tested the stacking procedure with simulations of dozens of Gaussian sources with fluxes below the 3σ limit randomly placed in the residual maps and we recovered, within a very good agreement, the input fluxes, therefore we find the method to be robust.

5.1 Non-detected, star-forming cluster members

To select the cluster members that are potentially star forming, we require that the individually undetected galaxies fulfil one of the three conditions: (i) show the [O II] emission line, (ii) have a late-type morphology and/or (iii) do not have red colour. We end up with nine potentially star-forming members not detected in either of the PACS bands.

The stacked flux in the 100 μm band is 0.65 mJy, a 2.6σ detection considering the new 3σ detection limit of $3 \times 0.75/\mathrm{sqrt}(N) = 0.75$ mJy. In the 160 μm band, we obtain a 3σ stacked flux of 1.6 mJy. The significance of these detections was tested with 1000 stacks of nine randomly placed sources in the residual maps. The average and standard deviation of the 1000 fluxes in both bands are a factor of 2–3 lower than our stacked flux measurements, therefore we are confident this is a real detection. Even though there is an

Table 2. Properties of the spectroscopically confirmed cluster members (first six rows) and photometric redshift members (seven rows after line break with suffix ‘p’ in ID) with *Herschel* detection. To measure the projected radial distance of the photometric members from the central galaxy in kpc, we assigned to those galaxies the cluster redshift, $z = 1.393$.

ID	RA (J2000)	Dec. (J2000)	z	Stellar mass ($\times 10^{10}$ M$_\odot$)	$L_{\rm IR}$ ($\times 10^{12}$ L$_\odot$)	SFR (M$_\odot$ yr^{-1})	Distance (kpc)	[O II]/Hα
5*	338.8407	−25.954 053	1.3986	2.0 ± 0.1	1.55 ± 0.19	268 ± 34	250	yes / yes
220	338.8212	−25.997 889	1.3879	4.8 ± 0.2	2.47 ± 0.32	427 ± 55	1210	yes / –
237*	338.8253	−25.968 533	1.3816	3.3 ± 0.2	0.57 ± 0.01	99 ± 2	414	yes / yes
1227*	338.8874	−25.965 951	1.3896	5.6 ± 0.2	1.27 ± 0.14	219 ± 25	1541	no / –
1863	338.8376	−26.022 967	1.3972	3.0 ± 0.1	1.28 ± 0.38	220 ± 66	1880	– / –
2669	338.8413	−25.917 121	1.3902	6.2 ± 0.2	0.77 ± 0.18	131 ± 33	1340	no / **
11p	338.8588	−25.988 553	1.38 ± 0.16	4.9 ± 0.2	2.71 ± 0.26	463 ± 44	1062	– / –
128p*	338.8651	−25.987 018	1.38 ± 0.24	5.3 ± 0.2	1.03 ± 0.16	176 ± 26	1165	– / –
157p	338.8236	−25.948 917	1.58 ± 0.19	2.5 ± 0.2	1.05 ± 0.16	180 ± 29	545	– / yes
225p*	338.8233	−25.935 927	1.64 ± 0.13	2.5 ± 0.2	1.35 ± 0.31	231 ± 54	869	– / **
246p	338.8534	−25.942 159	1.30 ± 0.06	1.8 ± 0.1	1.16 ± 0.22	199 ± 38	754	– / yes
300p	338.8485	−25.938 936	1.54 ± 0.15	2.1 ± 0.2	1.16 ± 0.33	198 ± 56	752	– / yes
301p*	338.8519	−25.953 788	1.50 ± 0.15	2.0 ± 0.2	0.52 ± 0.21	89 ± 35	508	– / **

[*] FIR emission likely contaminated by neighbour galaxies.

[**] Not in the Hα catalogue but the galaxy is at the edge of the NIRI FOV.

Table 3. *Herschel* fluxes in mJy of the spectroscopically confirmed cluster members (first six rows) and photometric redshift members (seven rows after line break with suffix ‘p’ in ID) with *Herschel* detection. The absence of error bars indicates the value is an upper limit.

ID	F_{100}	F_{160}	F_{250}	F_{350}	F_{500}
5	4.80 ± 0.34	11.14 ± 1.19	31.94 ± 6.84	30.79 ± 7.18	25.71 ± 7.61
220	11.77 ± 0.59	22.00 ± 1.00	31.31 ± 6.69	19.69 ± 6.94	14.51 ± 7.41
237	2.25 ± 2.25	6.62 ± 1.31	17.4	18.9	20.4
1227	2.25	9.6 ± 1.06	18.27 ± 6.44	11.94 ± 6.74	20.4
1863	6.6 ± 0.56	12.72 ± 0.9	17.4	18.9	20.4
2669	5.82 ± 0.45	4.9 ± 1.24	17.4	18.9	20.4
11p	13.6 ± 0.47	26.91 ± 1.24	29.40 ± 6.58	29.35 ± 7.08	16.90 ± 7.34
128p	5.72 ± 0.25	7.1 ± 0.93	12.16 ± 6.45	16.425 ± 6.85	9.88 ± 7.38
157p	4.92 ± 0.47	7.95 ± 0.9	17.4	18.9	20.4
225p	3.57 ± 0.47	9.45 ± 1.21	17.4	18.9	20.4
246p	3.22 ± 0.45	11.01 ± 0.88	23.07 ± 6.69	17.54 ± 6.83	18.48 ± 7.41
300p	2.33 ± 0.50	7.21 ± 1.07	11.21 ± 6.40	15.60 ± 6.85	13.85 ± 7.46
301p	2.27 ± 0.36	3.89 ± 0.88	17.4	18.9	20.4

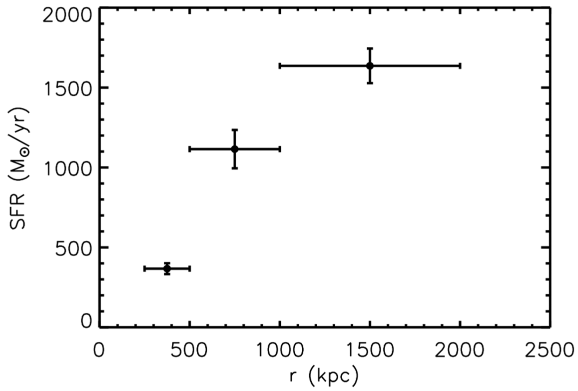

Figure 4. SFR versus radial distance from the cluster centre for the 13 cluster galaxies, distributed in three radial bins.

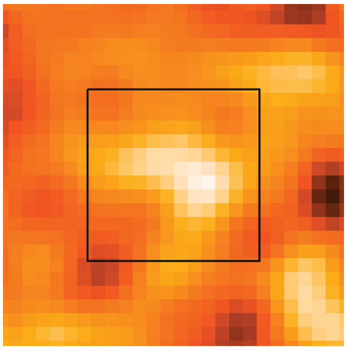

Figure 5. PACS 160 µm 1 arcmin × 1 arcmin, smoothed (Gaussian kernel of 7 arcsec) image of the stacked nine cluster members that individually are not detected by *Herschel*. The inner square has 30 arcsec × 30 arcsec.

uncertainty as to which galaxies the signal may come from, this method allows us to go below the nominal SF threshold of the observations and place an upper limit to the average SF of this sample of individually undetected sources. As expected, the stacking signal is stronger in the 160 µm (see Fig. 5) than at 100 µm, as the former is more sensitive to SF (i.e. closer to the SED peak) at the cluster redshift. We derive an SFR for the stacked sources of 48 ± 16 M$_\odot$ yr^{-1}, which is about half of the 3σ SFR limit for this cluster with the current data.

5.2 Non-detected narrow-band emitters

We have 25 narrow-band emitters with either a spectroscopic or a photometric redshift in accordance with the cluster redshift. In both the 100 and 160 µm maps, we have 20 non-detections of narrow-band emitters. At 100 µm the stacked flux is much below the 3σ limit obtained for the stacked image, which is 0.50 mJy. Similarly, in the 160 µm image the corresponding stacked flux is a factor of 8 below the 3σ detection which is 1.01 mJy. Based on these values we place an upper limit on the SF of the stacked non-detection of 24 $\mathrm{M}_\odot\ \mathrm{yr}^{-1}$, which is consistent with the average SFR derived from the Hα fluxes considering 2 mag in extinction.

6 THE sSFR–M_* RELATION

The SFR and sSFR have been shown to correlate with the galaxies stellar mass (M_*). These relationships provide clues to understand the origin of the reversal of the SF–density relation, observed to occur at $z \sim 1$ (Elbaz et al. 2007) in which distant galaxies show much larger typical SFR in dense environments (i.e. group range) relative to low-density environments. In this sub-section, we investigate how the SFR, sSFR and M_* correlate in XMM2235.

To compute the galaxy stellar masses we wish to probe the rest-frame 1.6 µm bump (Gavazzi, Pierini & Boselli 1996). At the cluster redshift, the 3.6 µm IRAC band corresponds to rest-frame 1.5 µm and is therefore the closest to the 1.6 µm emission. However, some of our galaxies are affected by blending in the IRAC bands, therefore we derive the stellar masses by scaling the observed K_s-band magnitudes using the conversion

$$M_* = (10.^{17.75\hat{E} - K_s \times 0.349})/0.62\,[\mathrm{M}_\odot] \qquad (2)$$

that was determined in Strazzullo et al. (2010) to convert the K-band luminosity function of blue sources (based on an appropriate colour selection) to the stellar mass function. We note that the calibration of the 3.6 µm mag versus stellar mass follows this relation very closely.

The sSFR, which is simply the SFR divided by the stellar mass, measures the SF efficiency of a galaxy and the fraction of the galaxy mass that can be converted into starlight per unit time. It has been shown that the sSFR increases with redshift independently of mass and the sSFR of massive galaxies is lower at all redshifts (Perez et al. 2008). Still, a degree of uncertainty and controversy exists in the details (slope and scatter) of these relations.

Elbaz et al. (2011) claim that high-redshift ULIRGS form stars in the so-called ‘normal’ main-sequence (MS) mode (see also Noeske et al. 2007), in contrast to the local ULIRGs that are mostly starbursts. The proposed redshift evolution of the sSFR of MS galaxies is parametrized in the following way:

$$\mathrm{sSFR}_{\mathrm{MS}}\ [\mathrm{Gyr}^{-1}] = 26 \times t_{\mathrm{cosmic}}^{-2.2}. \qquad (3)$$

For XMM2235, the age of the Universe at the cluster redshift is 4.62 Gyr which implies an $\mathrm{sSFR}_{\mathrm{MS}} = 0.9\ \mathrm{Gyr}^{-1}$. We draw this line in Fig. 6 and find that all of our individual detections are indeed above the MS line in the shaded region that corresponds to equation 14 of Elbaz et al. (2011) which defines the sSFR of a starburst as $>52 \times t_{\mathrm{cosmic}}^{-2.2}$. We ascribe this effect purely to a selection bias, as the SFR limit of these observations corresponds to $70(2\sigma)$–$105(3\sigma)$ $\mathrm{M}_\odot\ \mathrm{yr}^{-1}$, as indicated by the red dashed line in Fig. 6. This means that with the depth of these *Herschel* observations we can only detect sources above the MS. Only by stacking sources we can reach the MS level (see the magenta star symbol in Fig. 6).

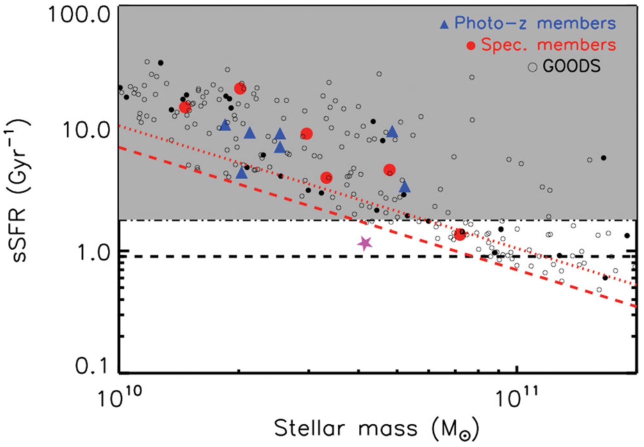

Figure 6. sSFR as a function of galaxy stellar mass for the spectroscopic members (red), photo-z members (blue) and for GOODS (black). The magenta star indicates the sSFR and average stellar mass of the stacked galaxies in Section 5. The dashed line corresponds to the relation found by Elbaz et al. (2011) representing the locus of the main sequence galaxies at the cluster redshift. The shaded area indicates the domain of starburst galaxies at $z = 1.393$. The sSFR detection limits of our data are shown by the red lines (2σ in dashed line, 3σ in dotted line).

To understand the role of environment in SF at high-redshift, we compare the FIR SFRs in this massive, biased system, with that of non-cluster fields observed with *Herschel* at the same depth and redshift. Only the very deep *Herschel* observations of the GOODS North and South fields obtained within the context of the PACS Evolutionary Probe (Lutz et al. 2011) have the necessary depth to directly compare the SF properties in low-density environments (i.e. fields) with respect to this cluster. Using the most recent catalogue of GOODS provided by the PEP consortium, we select a sub-sample of 33 field galaxies with spectroscopic redshifts in the range 1.35–1.45, and 255 photometric redshifts galaxies within the same redshift interval used for the cluster (i.e. 1.1–1.7) for which we have stellar masses, L_{IR} and SFR above our 2σ detection limit in the cluster.

We find that the field starburst galaxy population with a similar redshift of XMM2235 occupies the same region of our cluster in the SFR – M_* and sSFR – M_* relations, as shown in Fig. 6.

7 AGNS IN THE CLUSTER

The number and distribution of AGNs in clusters provides important clues on the growth of the supermassive black holes at the centres of clusters, the nature of AGN fuelling, and the impact of AGNs on the intracluster medium over cosmic time. Moreover, the numerous arguments that support a connection between SF and black hole accretion indicate that there should be an increased AGN population in distant clusters. Few studies have investigated the number and evolution of AGNs in clusters in a systematic way and using a statistically significant sample (Galametz et al. 2009; Martini, Sivakoff & Mulchaey 2009, and more recently Martini et al. 2013). Specifically, Martini et al. (2009), quantifies the evolution of the fraction of luminous X-ray AGNs in clusters from $f_A = 0.13^{+0.18}_{-0.087}$ per cent at $z = 0.2$ to $f_A = 1.00^{+0.29}_{-0.23}$ per cent at $z = 0.7$, or more simply, a factor of 8 increase to $z = 1$.

Using the sub-arcsecond resolution data from *Chandra*, we identify point source X-ray emission from AGNs associated with the cluster members ID 5, 237, 1227 and 2669, all of them with FIR emission. The X-ray luminosities of these AGNs span the range

0.8–6.7 × 10^{43} erg s^{-1} in the hard band (2.0–10 keV), that corresponds to type 2 (obscured) AGN.

We attempt to estimate the contribution of the AGNs associated with these four galaxies to the FIR luminosity by performing a decomposition of the SEDs with DECOMPIR,[1] a program that separates infrared SEDs into their AGN and host-galaxy components (Mullaney et al. 2011). While for ID 5, 237 and 1227, the fit appears to be entirely dominated by the host galaxy, for ID 2669 there is a hint for an AGN component that dominates the FIR bump. We argue that we have a tentative case for AGN contamination in this cluster member, since this isolated galaxy has $F_{100\,\mu\mathrm{m}} > F_{160\,\mu\mathrm{m}}$, which is best explained if we consider emission by an AGN. However, given the large uncertainties of this fit caused by the poor data at 250/350/500 μm, we unable to quantify the FIR emission due to the AGN. Using the FIR luminosities computed with LEPHARE in Section 4, we tentatively find an anticorrelation between the X-ray and FIR luminosities for these four galaxies.

8 MORPHOLOGIES

The morphological type of a galaxy is tightly correlated with its SF activity (e.g. Wuyts et al. 2011; Bell et al. 2012). Star-forming galaxies are typically associated with late-types (mostly spirals and irregulars) whereas early-types (ellipticals and spheroidals) – the predominant class in massive clusters – are mostly passive, ‘red and dead’ galaxies, at least up to $z \leq 2$. Using the high angular resolution of *HST*, we can determine the morphological classification of these small, distant galaxies, either by a visual comparison with reference templates (e.g. Postman et al. 2005 for high-redshift galaxies) or by fitting surface brightness models (e.g. Sérsic, de Vaucouleurs models) to the data, and studying the distributions of the output parameters (e.g. Blakeslee et al. 2006). We perform here a visual classification of the morphological type of the members with PACS detection and therefore a high SFR. All seven photometric-redshift members have coverage with ACS; however, only two of the six spectroscopic members were imaged with *HST*. We present in Fig. 7 postage stamps of these galaxies using the ACS/F850LP band. As expected, most if not all galaxies have a complex morphology with irregular features, typical of late-types. About half of the galaxies in this sample (ID 5, 157p, 225p) show signs of on-going mergers, the preferred mechanism to explain starbursts. We note that galaxy ID 237 (which is located very close to a bright star) shows X-ray point source emission.

9 CANDIDATE CLUSTER MEMBERS SELECTED IN PACS DATA

In addition to the study of the sources for which we have redshift information (either from spectroscopy or photometric redshifts), we exploit the full FOV of the PACS images to perform a more general selection of FIR sources that are likely to be highly star-forming candidates. This selection follows from the assumption that the peak of the SED is at ∼240 μm for a starburst at the cluster redshift (see e.g. Kirkpatrick et al. 2012; Casey 2012), which allows us to define the simple colour criterion F250 > F160 > F100 μm. We chose not to add the condition F350 < F250 in our selection, due to the poor resolution of SPIRE at long wavelengths.

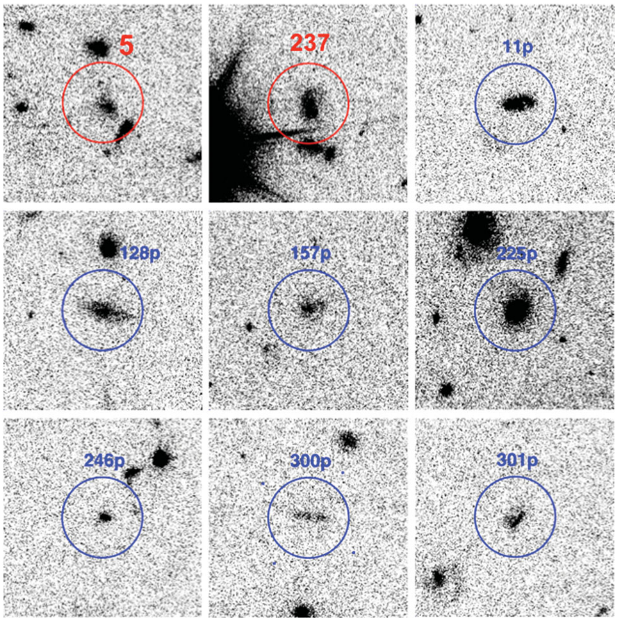

Figure 7. *HST*/ACS-F850 10 arcsec × 10 arcsec stamps of two spectroscopic cluster members (ID 5, 237) and seven photo-z members of XMM2235, used to assess the morphologies of these galaxies with emission in PACS. The circles have a radius of 2 arcsec.

A total of 60 sources (of the 158 3σ sources in the matched 100–160 μm catalogue) meet our selection criteria. Of these, eleven PACS candidates are found to be spectroscopic interlopers, three more are photo-z interlopers, and after a visual screening of the individual galaxies in the PACS and the K_s-band data we discard five additional sources which are considered spurious or for which we have a low S/N. Of the remaining 41 sources listed in Table 4, one is the spectroscopic member ID 5, and six have a photometric redshift within a range of 0.15 from the cluster redshift.

We note that not all cluster members listed in Table 2 are included in this sample, since for most of those cluster galaxies we do not have 3σ fluxes in both PACS bands. Nonetheless, we confirm that generally their SEDs satisfy our flux selection criterion, with the exception of ID 2669, which has $F_{160} = 4.9 \pm 1.24$ mJy and $F_{100} = 5.82 \pm 0.45$ mJy. This is likely explained by the presence of an AGN component as shown in Section 7, which boosts the 100 μm flux.

To estimate the contamination in this sample, we use the photometric redshift catalogue, which is less prone to selection biases. We find 10 photo-z galaxies in the initial catalogue of 60 PACS selected sources, of these six are photo-z member candidates, and four are photo-z interlopers, i.e., their redshift is outside the range [1.1–1.7]. Two of the four photo-z interlopers are also spectroscopic interlopers. Even though this is a rough estimate, we consider a contamination of 40 per cent in our sample of purely infrared selected cluster candidates. This number may be higher though, because the photometric redshifts have an expected fraction of spurious sources of 50 per cent.

All candidates are located outside the cluster core ($r > 250$ kpc) and ∼85 per cent are beyond R_{500} in the range of 1–3 Mpc from the BCG. Since we do not have photometric redshifts for a large part of this sample as most of our optical data is limited to the inner few arcminutes, we assign to all candidates the cluster redshift and perform an FIR SED fitting analysis to obtain the total LIR and SFR. The results of this analysis are listed in Table 4. The best approach to confirm this sample is to have NIR spectroscopy follow-up.

---

[1] https://sites.google.com/site/decompir/

Table 4. FIR properties of PACS selected cluster member candidates.

ID	RA (J2000)	Dec. (J2000)	L_{IR} ($\times 10^{12}$ $\mathrm{L}_{\odot}$)	SFR ($\mathrm{M}_{\odot}$ yr^{-1})	Distance (arcmin)
10p	338.730 068 70	−25.985 957 20	3.40 ± 0.30	244 ± 50	6.6
11p*	338.858 478 80	−25.988 518 50	2.71 ± 0.26	463 ± 44	2.1
38p	338.872 199 89	−26.007 034 30	2.38 ± 0.47	406 ± 80	3.5
44p	338.798 764 60	−25.930 981 20	2.27 ± 0.33	387 ± 57	2.9
45p	338.849 948 60	−25.932 862 89	1.80 ± 0.34	309 ± 59	1.9
49p	338.868 127 00	−26.008 026 90	2.21 ± 0.37	376 ± 64	3.4
53p	338.802 069 50	−25.977 944 99	1.41 ± 0.32	242 ± 56	2.3
54p	338.784 488 80	−25.917 539 60	1.92 ± 0.34	330 ± 57	4.1
64p	338.842 164 20	−25.893 364 20	2.07 ± 0.39	354 ± 66	4.1
72p	338.906 874 59	−25.946 951 99	2.40 ± 0.50	410 ± 86	4.3
78p	338.813 354 30	−25.933 542 80	1.48 ± 0.43	252 ± 72	2.2
80p	338.746 497 40	−25.930 004 79	3.25 ± 0.37	556 ± 63	5.7
81p	338.748 889 79	−25.955 011 59	1.69 ± 0.33	289 ± 57	5.3
84p	338.815 758 00	−25.877 025 19	1.39 ± 0.28	238 ± 48	5.2
103p	338.849 484 70	−25.910 158 70	1.50 ± 0.29	256 ± 50	3.1
106p	338.818 991 99	−25.996 357 19	1.74 ± 0.40	298 ± 68	2.4
107p	338.903 472 70	−25.928 482 29	2.09 ± 0.36	358 ± 61	4.4
111p	338.854 146 89	−26.057 692 40	2.38 ± 0.33	407 ± 57	5.9
116p	338.812 770 10	−26.008 599 30	1.45 ± 0.35	248 ± 59	3.2
128p*	338.864 929 19	−25.986 684 79	1.03 ± 0.16	176 ± 26	2.3
142p	338.859 456 59	−25.932 658 29	1.63 ± 0.39	279 ± 67	2.2
148p	338.914 335 99	−25.940 826 39	1.28 ± 0.21	219 ± 37	4.8
153p	338.910 980 99	−25.994 188 20	3.2 ± 0.30	142 ± 40	4.9
160p*,**$^{+}$ = ID5	338.840 484 61	−25.953 567 50	1.55 ± 0.19	268 ± 34	0.5
162p	338.869 389 00	−25.925 095 29	1.35 ± 0.28	232 ± 49	2.9
165p	338.850 214 30	−26.059 124 19	1.71 ± 0.32	293 ± 55	5.9
170p	338.885 312 80	−25.918 036 69	0.77 ± 0.32	132 ± 56	3.9
172p	338.772 269 90	−25.971 742 50	0.63 ± 0.21	107 ± 45	3.9
181p	338.838 159 80	−25.890 497 40	1.58 ± 0.33	270 ± 57	4.2
188p	338.772 789 40	−25.985 064 69	1.53 ± 0.29	261 ± 51	4.1
192p	338.905 472 99	−25.993 968 29	1.63 ± 0.32	279 ± 55	4.6
208p	338.901 873 20	−25.963 280 69	1.23 ± 0.28	211 ± 49	3.9
218p	338.890 786 60	−25.964 787 00	1.29 ± 0.39	222 ± 67	3.2
219p	338.811 495 20	−25.940 314 09	0.68 ± 0.18	115 ± 31	2.0
243p	338.850 180 20	−26.007 476 60	0.96 ± 0.25	164 ± 42	2.9
246p**$^{,+}$	338.853 240 96	−25.941 967 01	1.16 ± 0.22	199 ± 38	1.5
252p	338.861 907 95	−25.930 784 22	1.51 ± 0.44	259 ± 75	2.4
300p*$^{+}$	338.848 327 63	−25.939 178 46	1.16 ± 0.33	198 ± 56	1.5
301p*	338.852 264 40	−25.953 863 14	0.52 ± 0.21	89 ± 35	1.0
304p^{+}	338.857 482 91	−25.949 279 78	0.95 ± 0.28	162 ± 47	1.4
327p	338.759 336 09	−25.981 576 00	1.47 ± 0.27	251 ± 47	4.8

* photo-z member, ** spectroscopic cluster member, $^{+}$ narrow-band emitter.

The PACS candidates and Hα emitter catalogues overlap within a very small FOV (see Fig. 8) that includes only 9 PACS candidates. Of these, four galaxies are present in both catalogues. The remaining five PACS candidates that are not seen in Hα may be either interlopers or strongly obscured. The sensitivity of the *Herschel* maps allows us to detect only the high star-forming galaxies, so we miss the low SFR galaxies that constitute the bulk of the Hα detections. Several studies have reported high ($A_{H\alpha} \sim 3$ mag) extinction levels when comparing mid- or FIR sources with Hα emitters with similar stellar mass in high-redshift clusters (e.g. Koyama et al. 2011). In the following section we estimate the extinction in Hα.

9.1 SFR(Hα) versus SFR(FIR)

We compare the SFRs obtained via the Hα luminosity as presented by Grützbauch et al. (2012), with our SFRs measured by integrating the FIR luminosities, L_{IR}, and applying the Kennicutt (1998) law. To perform this comparison, we use a set of six galaxies with both SFR(Hα) and SFR(FIR) measurements, for which we have either a spectroscopic or a photometric redshift. This is a small sample in part because the overlapping FOV is small (∼5 arcmin × 3.5 arcmin), and because the depth of our *Herschel* images corresponds into a minimum SFR of the order of 70 (2σ)–$105(3\sigma)$ $\mathrm{M}_{\odot}$ yr^{-1}, not allowing us to detect low star-forming galaxies.

We find that the quoted SFR(Hα) is systematically lower than the corresponding SFR(FIR), SFR(Hα) ∼ 0.1–0.2 SFR(IR). The amount of extinction in Hα needed to reconcile these two independent SF diagnostics is 3 mag, a reasonable value for the range of SFR spanned by our galaxies (e.g. Koyama et al. 2011). Also recent work by Ibar et al.(in preparation) found a similar trend when comparing the SFR(Hα) with SFRs obtained from *Spitzer*–MIPS or *Herschel* using a sample of field galaxies at $z = 1.47$.

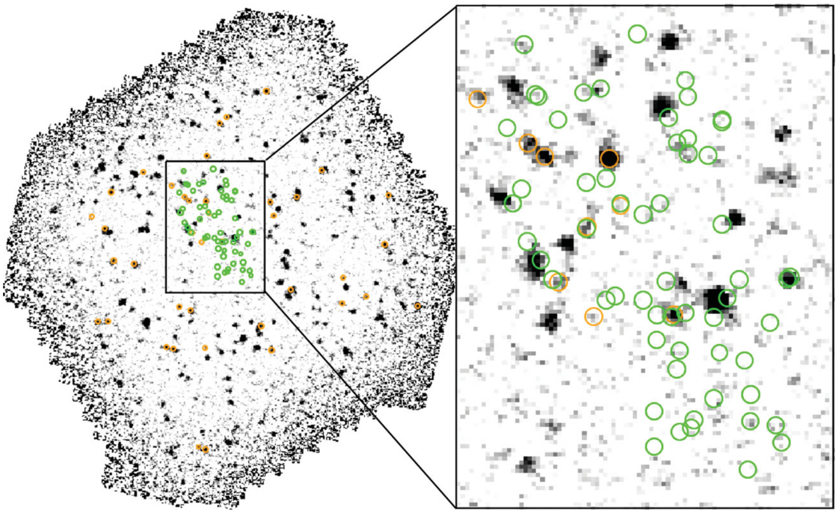

Figure 8. PACS selected cluster member candidates (orange) and Hα emitters (green). The black square indicates the overlapping FOV with 3 arcmin × 4 arcmin.

10 SINFONI IFU DATA OF THE BCG: UPPER LIMIT ON Hα EMISSION

XMM2235 is currently the most distant cool-core cluster on the basis of its X-ray properties (i.e. surface brightness concentration $c_{\rm SB}$, short cooling time and a hint of a temperature drop towards the core) that were studied in detail using deep *Chandra* data in Rosati et al. (2009). Besides these well-known X-ray properties, the cool-core phenomenon sometimes also manifests in the central galaxy through SF caused by the inflow of cold gas in the cluster centre. Indeed, Cavagnolo et al. (2008) demonstrated that local clusters with low central entropy (which is closely related to the central cooling time) derived from their X-ray surface brightness properties have a high probability to have a BCG with optical line emission. However, the effect of SF induced by cooling in otherwise red, passive elliptical galaxies is very challenging to measure, with reported fractions of BCGs with [O II] emission of the order of 35 per cent in local cool-cores (Donhaue et al. 2010). At high redshifts measuring this effect is even more challenging due to the faintness of distant galaxies. Moreover, we may observe and measure X-ray quantities that show that a cluster is a cool-core, however, the triggering of SF in the BCG may be delayed and thus absent.

The measurement of SF in the central galaxies of cool-core clusters using *Herschel* is limited to low redshift clusters (e.g. Mittal et al. 2012) due to the high SF thresholds imposed by the *Herschel* data. Still, Rawle et al. (2012) recently conducted a study in BCGs up to $z = 1$ and found that star-forming BCGs require a small (<1 mag) extinction correction to reconcile SFR(Hα) with SFR(FIR) which should be linked to a different source of fuel (cold gas) other than the normal stellar mass loss.

The BCG of XMM2235 is a very large and massive elliptical galaxy ($\sim 10^{12}\,{\rm M}_{\odot}$) perfectly centred with respect to the peak of the X-ray emission. We were awarded with a 7 h IFU spectroscopy of the BCG using the NIR spectrograph SINFONI at European Southern Observatory (ESO)/VLT (Bonnet et al. 2004; Eisenhauer et al. 2010), to investigate the presence of Hα emission in the central galaxy as a tracer of SF (PI Santos, 383.A-0825A). The observations were taken in 2009 August, in non-AO mode with an on-source exposure of 5 h in the 8 arcsec × 8 arcsec field. We performed a standard data reduction and obtain the final spectrum by median stacking of the individual spectra.

We do not detect any convincing Hα emission, hence we report a 3σ upper limit on the Hα flux in the XMM J2235−25 BCG of 9×10^{-17} erg s^{-1} cm^{-2}. This translates to an upper limit on the SFR of $7.6\,{\rm M}_{\odot}\,{\rm yr}^{-1}$ for Kennicutt (1998) with a Salpeter IMF, assuming a line width of 150 km s^{-1} and no reddening correction. This upper limit is a factor 10 lower than the one we can place with the current *Herschel* data.

11 CONCLUSIONS

In this paper, we have characterized the FIR properties of the galaxies (confirmed and photo-z candidates) in XMM2235, a massive cluster at $z = 1.4$, using deep *Herschel* imaging data from 100 to 500 µm. The extensive ancillary data of this cluster is crucial to ensure a proper identification of the cluster galaxies in the *Herschel* maps, and to further characterize the properties of the highly star-forming members. We summarize our main results here:

(i) we derived SFRs for the 13 spectroscopic and photo-z members in the range 89–463 ${\rm M}_{\odot}\,{\rm yr}^{-1}$, all of them lie outside the core at $r > 250$ kpc from the centre and extend well beyond R_{500};

(ii) we obtained a significant stacking signal of nine spectroscopic members that were not individually detected by PACS, corresponding to a SFR $= 48 \pm 16\,{\rm M}_{\odot}\,{\rm yr}^{-1}$;

(iii) we find that four of the six spectroscopic members detected by PACS are associated with AGN X-ray emission, although the data did not allow for a decomposition of the FIR emission into an AGN and host components;

(iv) we performed a visual morphological classification of a subsample of nine members with *HST*/ACS data which show that these high star-forming galaxies are all late-types;

(v) we find that SFR (Hα) is a factor of 5–10 lower than SFR (IR), which indicates that a dust extinction of about 3 mag in Hα;

(vi) the sSFR–M_* relation shows that all cluster members with FIR emission are starburst galaxies that follow the same trend as field galaxies at the same redshift;

(vii) we selected a sample of 41 FIR cluster member candidates using a colour criterion based on the shape of the SED. To confirm these are highly star-forming members we require follow-up observations in the NIR.

We also presented deep IFU SINFONI data of the BCG, with the aim to detect Hα emission since this is a cool-core cluster. We place a strict upper limit of 7.6 $M_{\odot}$ yr^{-1} to the Hα-derived SF, which is much below the upper limit we can place using the FIR data. The lack of Hα emission in the massive, large, central galaxy implies that the SF induced by the cold gas in the core has not started yet (since this is a very distant cluster) or already happened on a short time-scale.

Even though this is currently the deepest *Herschel* data of a distant galaxy cluster, the FIR study of the individual cluster members is still quite challenging because the poor resolution of the data makes it hard to disentangle contamination from undesired objects. Furthermore, only highly star-forming galaxies can be detected with this data, i.e. our 2σ (3σ) limit on the SFR is 70(105) $M_{\odot}$ yr^{-1}, allowing us to detect mostly ULIRGS. Stacking cluster members proved to be an important resource to go below the nominal SFR limit and reach the MS level. Nevertheless, follow-up observations in the NIR (ideally multi-object spectroscopy) targeting the Hα emission line covering the large FOV of PACS are needed to confirm the cases where there is significant contamination and to confirm the large sample of PACS selected cluster galaxy candidates.

At $z = 1.4$, we do not witness a reversal of the SFR–density relation in this massive cluster. As shown in Fig. 4, all cluster members with FIR emission and PACS selected candidates are located at a radius greater than 250 kpc from the cluster centre. Six of the 13 individual detections are beyond a radius of 1 Mpc, approximately the cluster virial radius, therefore most of the measured FIR SF in this cluster occurs in potentially infalling galaxies at the edge of the cluster X-ray emission. We note, however, that current studies providing evidence for an increase of SF in the centres of distant clusters used MIPS 24 μm data and thus had a lower limit to the SFR.

The study presented here on the individual system XMM2235 is part of a larger project including more than a dozen galaxy clusters reaching the proto-cluster regime, that will allow us to characterize SF activity at different cosmic times and stages of evolution.

ACKNOWLEDGEMENTS

JSS thanks D. Elbaz and R. Gobat for useful discussions and R. Grützbauch for sending us the yet unpublished catalogue of revised SFR of the Hα emitters. RD acknowledges the support provided by the BASAL Center for Astrophysics and Associated Technologies and by FONDECYT N. 1100540. CL is the recipient of an Australian Research Council Future Fellowship (programme number FT0992259).

PACS has been developed by a consortium of institutes led by MPE (Germany) and including UVIE (Austria); KUL, CSL, IMEC (Belgium); CEA, OAMP (France); MPIA (Germany); IFSI, OAP/AOT, OAA/CAISMI, LENS, SISSA (Italy); IAC (Spain). This development has been supported by the funding agencies BMVIT (Austria), ESA-PRODEX (Belgium), CEA/CNES (France), DLR (Germany), ASI (Italy) and CICYT/MCYT (Spain).

SPIRE has been developed by a consortium of institutes led by Cardiff University (UK) and including University of Lethbridge (Canada); NAOC (China); CEA, LAM (France); IFSI, University of Padua (Italy); IAC (Spain); Stockholm Observatory (Sweden); Imperial College London, RAL, UCL-MSSL, UK ATC, University of Sussex (UK); Caltech, JPL, NHSC, University of Colorado (USA). This development has been supported by national funding agencies: CSA (Canada); NAOC (China); CEA, CNES, CNRS (France); ASI (Italy); MCINN (Spain); SNSB (Sweden); STFC and UKSA (UK); and NASA (USA).

Based on observations made with the European Southern Observatory (ESO) telescopes at Paranal Observatories under programme ID 383.A-0825(A), 274.A-5024(B), 077.A-0177(A, B), 074.A-0023(A), 077.A-0110(A, B).

REFERENCES

Arnouts S., Cristiani S., Moscardini L., Matarrese S., Lucchin F., Fontana A., Giallongo E., 1999, MNRAS, 310, 540
Bauer A. E., Grützbauch R., Jørgensen I., Varela J., Bergmann M., 2011, MNRAS, 411, 2009
Bavouzet 2008, PhD Thesis Univ. Paris Sud 11 (http://tel.archives-ouvertes.fr/tel-00363975/fr/)
Bell E. F. et al., 2012, ApJ, 753, 167
Berta S. et al., 2011, A&A, 532, A49
Béthermin M., Dole H., Beelen A., Aussel H., 2010, A&A, 512, A78
Blakeslee J. P. et al., 2006, ApJ, 644, 30
Bonnet H. et al., 2004, ESO Messenger 117, 17
Bruzual G., Charlot S., 2003, MNRAS, 344, 1000
Casey C. M., 2012, MNRAS, 425, 3094
Cavagnolo K. W., Donahue M., Voit G. M., Sun M., 2008, ApJ, 683, L107
Chary R., Elbaz D., 2001, ApJ, 556, 562
Coia D. et al., 2005, A&A, 431, 433
De Lucia G., Fontanot F., Wilman D., Monaco P., 2011, MNRAS, 414, 1439
Diolaiti E. et al., 2000, in Manset N., Veillet C., Crabtree D., eds, ASP Conf. Ser. Vol. 216, Astronomical Data Analysis Software and Systems IX. Astron. Soc. Pac., San Francisco, p. 623
Dole H. et al., 2006, A&A, 451, 417
Donahue M. et al., 2010, ApJ, 715, 881
Dressler A., 1980, ApJ, 236, 351
Eisenhauer F. et al., 2003, SPIE, 4841, 1548
Elbaz D. et al., 2007, A&A, 468, 33
Elbaz D. et al., 2011, A&A, 533, A119
Fassbender R. et al., 2011, New J. Phys., 13, 125014
Galametz A. et al., 2009, ApJ, 694, 1309
Gavazzi G., Pierini D., Boselli A., 1996, A&A, 312, 397
Griffin M. J. et al., 2010, A&A, 518, L3
Grützbauch R., Bauer A. E., Jørgensen I., Varela J., 2012, MNRAS, 423, 3652
Haines C. P., Gargiulo A., La Barbera F., Mercurio A., Merluzzi P., Busarello G., 2007, MNRAS, 381, 7
Hayashi M., Kodama T., Koyama Y., Tanaka I., Shimasaku K., Okamura S., 2010, MNRAS, 402, 1980
Heckman T. M., Baum S. A., van Breugel W. J. M., McCarthy P., 1989, ApJ, 338, 48
Hilton M. et al., 2010, ApJ, 718, 133
Hopkins P. F., Cox T. J., Kereš D., Hernquist L., 2008, ApJS, 175, 390
Ilbert O. et al., 2006, A&A, 457, 841
Jee et al., 2009, ApJ, 704, 672
Kennicutt R. C., Jr, 1998, ARA&A, 36, 189
Kewley, Geller M. J., Jansen R. A., Dopita M. A., 2002. AJ, 124, 3135
Kirkpatrick A. et al., 2012, ApJ, 759, 139
Koyama Y., Kodama T., Nakata F., Shimasaku K., Okamura S., 2011, ApJ, 734, 66
Lemaux B. C., Lubin L. M., Shapley A., Kocevski D., Gal R. R., Squires G. K., 2010, ApJ, 716, 970
Lidman C. et al., 2008, A&A, 489, 981
Lutz D. et al., 2011, A&A, 532, A90
Martini P., Sivakoff G. R., Mulchaey J. S., 2009, ApJ, 701, 66
Martini P. et al., 2013, ApJ, 768, A1
Metcalfe L., Fadda D., Biviano A., 2005, Space Sci. Rev., 119, 425
Mittal R. et al., 2012, MNRAS, 426, 2957
Mullaney J. R., Alexander D. M., Goulding A. D., Hickox R. C., 2011, MNRAS, 414, 1082

Mullis C. R., Rosati P., Lamer G., Böhringer H., Schwope A., Schuecker P., Fassbender R., 2005, ApJ, 623, L85

Nguyen H. T. et al., 2010, A&A, 518, L5

Noeske K. G. et al., 2007, ApJL, 660, L43

Ott S. et al., 2006, in Gabriel C., Arviset C., Ponz D., Solano E., eds, ASP Conf. Ser. Vol. 351, Astronomical Data Analysis Software and Systems XV., Astron. Soc. Pac, San Francisco, p. 516

Pérez-González P. G. et al., 2008, ApJ, 675, 234

Pilbratt G. L. et al., 2010, A&A, 518, L1

Poglitsch A. et al., 2010, A&A, 518, L2

Popesso P. et al., 2011, A&A, 532, A145

Popesso P. et al., 2012, A&A, 537, A58

Postman M. et al., 2005, ApJ, 623, 721

Rawle T. D. et al., 2012, ApJ, 747, 29

Rosati P. et al., 2009, A&A, 508, 583

Saintonge A., Tran K.-V. H., Holden B. P., 2008, ApJ, 685, L113

Seymour N. et al., 2012, ApJ, 755, 146

Smith A. J. et al., 2012, MNRAS, 419, 377

Strazzullo V. et al., 2010, A&A, 524, A17

Tran K.-V. H. et al., 2010, ApJ, 719, L126

Treu T., Ellis R. S., Kneib J.-P., Dressler A., Smail I., Czoske O., Oemler A., Natarajan P., 2003, ApJ, 591, 53

Wuyts S. et al., 2011, ApJ, 742, 96

This paper has been typeset from a TEX/LATEX file prepared by the author.